The Origin of High Mobility in Molybdenum Doped Indium Oxide

Davinder S. Bhachu,[1*] David O. Scanlon,[2,3] Gopinathan Sankar,[1] T. D. Veal,[4] Russell G. Egdell,[5] Giannantonio Cibin,[3] Andrew J. Dent,[3] Caroline E. Knapp,[1] Claire J. Carmalt[1] and Ivan P. Parkin[1*]

*Corresponding author

[1]Materials Chemistry Centre, Department of Chemistry, University College London, 20 Gordon Street, London WC1H 0AJ, UK

[2]University College London, Kathleen Lonsdale Materials Chemistry, Department of Chemistry, 20 Gordon Street, London, WC1H 0AJ, UK

[3]Diamond Light Source Ltd., Diamond House, Harwell Science and Innovation Campus, Didcot, Oxfordshire OX11 0DE, UK

[4]Stephenson Institute for Renewable Energy and Department of Physics, School of Physical Sciences, University of Liverpool, Liverpool, L69 7ZF, UK

[5]Chemistry Research Laboratory, Mansfield Road, Oxford OX1 3TA, United Kingdom

Abstract

Molybdenum doped indium oxide (IMO) thin films prepared by aerosol assisted chemical vapour deposition (AACVD) show significantly improved charge carrier mobilities as compared to nominally undoped films prepared by the same technique. The basis for this very unusual behaviour has been investigated by density functional theory calculations using a hybrid Hamiltonian, mobility modelling, X-ray photoemission and X-ray absorption spectroscopies. In contrast to previous claims that Mo acts as a three-electron donor, it is shown that

substitutional Mo traps two electrons in localised states falling within the bulk bandgap and thus Mo is a simple one-electron donor. At the same time there is very little hybridisation of Mo 4d states with In 5s states at the bottom of the conduction band. This results in conduction that is spatially separated to some degree from the donors, giving rise to significantly reduced ionized impurity scattering, enhancing the carrier mobility. This is in contrast to Sn-doped In_2O_3 where the conduction band minimum has significant Sn 5s character, resulting in regular ionized impurity scattering.

Keywords: Indium Oxide, transparent conducting oxide, thin films, AACVD

* Fax: (+44) 20-7679-7463 E-mail: i.p.parkin@ucl.ac.uk

1. Introduction

Indium oxide (In_2O_3) is amenable to degenerate n-type doping with tin to give a transparent conducting oxide (TCO) that combines optical transparency in the near infrared and visible regions with a high electrical conductivity.[1] So-called indium tin oxide or ITO is still the most widely used conducting window material in photovoltaic devices, liquid crystal displays and light emitting diodes, despite the high material cost of indium.[2–6] This is a consequence of a relatively small fundamental bandgap which allows the charge neutrality level to fall well above the conduction band minimum, thus ensuring a high intrinsic dopability.[7] At the same time optical transitions from the top of the valence band into the conduction band have very low oscillator strength so that indium oxide and ITO thin films remain transparent across the whole of the visible region.[8] The optimal room

2

temperature electron mobility for nominally undoped indium oxide as found in high quality thin films grown on (111) oriented yttrium-doped zirconium dioxide substrates by oxygen plasma assisted molecular beam epitaxy is around 225 $cm^2V^{-1}s^{-1}$.[9] Carrier concentrations of the order 10^{17} cm^{-3} found in these materials arise from adventitious donor doping, attributed to oxygen vacancies.[9] As is usual in semiconductor systems, n-type doping with an element (Sn) to the right of the host (In) in the periodic table leads to an increase in the charge carrier concentration, but also to a decrease in carrier mobility to values around 70 $cm^2V^{-1}s^{-1}$ for carrier densities in the mid 10^{20} cm^{-3} range.[1] The latter is a consequence of the fact that the states close to the conduction band minimum have a strong contribution from the Sn 5s orbitals of the dopant atoms so that there is pronounced ionised impurity scattering.

A common problem with heavily doped TCO materials is that the conduction electron plasmon energy lies in the near IR region, limiting the window of optical transparency.[10–16] Immediately above the plasmon energy a TCO material is transparent but below the film is highly reflecting. In addition there is strong absorption around the plasmon energy itself and this may intrude on the visible region at high carrier densities, especially for materials with low mobility where the plasma edge is strongly broadened by carrier lifetime effects. For this reason high conductivity is best achieved by combining high mobility with relatively low carrier densities, rather than with high carrier densities and relatively low mobility.

Against this background there has been a growing interest in the past few years in In_2O_3 films incorporating alternative transition metal dopants including Mo, W, Nb and Ti.[10–16] Mo has been of particular interest due to the remarkably

high mobilities that have been found even in polycrystalline films. Thus Gupta et al. claimed a mobility of 250 cm^{2}V^{-1}s^{-1} at a carrier density of 3.5×10^{20} cm^{-3} in thin films containing 2 atomic % Mo grown by pulsed laser deposition on quartz substrates held at 500 °C under a background oxygen pressure of 10^{-3} mbar.[17] This is an even higher mobility than the 226 cm^2/Vs reported for a high-quality, single crystalline, undoped In$_2$O$_3$ thin film grown by plasma-assisted molecular beam epitaxy for an electron concentration of only 5×10^{16} cm^{-3}.[23] The reason why the mobility in a polycrystalline film can exceed that found in epitaxial films of the highest quality remains unclear, however, although it is widely believed that Mo can act as a three electron donor and it has therefore been argued that the ratio between charge carriers and scattering centres should be lower than with single electron donors such as Sn.[24] Although ionized impurity scattering-limited mobility for triply charged donors is expected to be one third that for singly charged donors, if all other properties are equal.[25]

In the present study Mo:In$_2$O$_3$ films were prepared on silica coated float glass substrates by aerosol assisted chemical vapour deposition (AACVD). Mo/In in the precursor solution was varied from 1-7 mol.%. To compare against Mo:In$_2$O$_3$ samples, Sn-doped In$_2$O$_3$ (Sn/In in precursor solution kept at 2 mol.%) was also prepared by AACVD. It emerges that the Mo doped films prepared in this way have a carrier concentrations of between 3×10^{20} cm^{-3} and 7×10^{20} cm^{-3}, up to a factor of 7 higher than for nominally undoped films prepared by the same technique. At the same time the mobility of the charge carriers *increases* from 71 cm^{2}V^{-1}s^{-1} for nominally undoped films to up to 119 cm^{2}V^{-1}s^{-1} for a carrier density of 4.4×10^{20} cm^{-3} The latter mobility value is remarkably high for a polycrystalline film prepared by a relatively crude deposition technique at this carrier density.

For the highest carrier density obtained of 7×10^{20} cm^{-3}, the mobility is only reduced to 109 cm^{2}V^{-1}s^{-1} producing a very low resistivity of 8.3×10^{-5} Ωcm. Mo:In$_2$O$_3$ with Mo/In kept at 2 mol.% in the precursor solution showed the highest charge carrier mobility. Thus, a Sn:In$_2$O$_3$ thin films with Sn/In kept at 2 mol.% was synthesised as a comparison. To help explain the surprising increase in mobility with Mo doping we have carried out density functional theory calculations using a hybrid Hamiltonian which faithfully reproduces the bulk band gap of In$_2$O$_3$ itself. Unlike in previous calculations which used the local density approximation,[26] we find that each Mo dopant atom traps 2 electrons in localised Mo 4d states lying in the bulk band gap so that Mo acts as a single rather than triple electron donor. These localised states are seen directly in valence band X-ray photoemission spectra. Additionally, there is exchange splitting of the Mo 4d states so that the conduction electrons of one spin are only scattered by half the Mo dopants. Thus in contrast to Sn-doped In$_2$O$_3$, the ionized impurity scattering is significantly reduced, enhancing the carrier mobility.

2. Experimental and Computational Details

Deposition Procedure

Depositions were carried out under nitrogen (99.99% from BOC). Precursors were placed in a glass bubbler and an aerosol mist was created using a piezoelectric device.[27–30] All chemicals were procured from Aldrich and were used as received.

Mo:In2O3 thin films were prepared from InCl$_3$.H$_2$O (0.4 g, 8.8 mmol) dissolved in methanol (25 ml) and (NH$_4$)$_6$Mo$_7$O$_{24}$.4H$_2$O was added (1, 2, 3, 4, 5 and 7 mol.%). As a comparison an Sn:In$_2$O$_3$ thin film was prepared from InCl$_3$.H$_2$O (0.4

g, 8.8 mmol) dissolved in methanol (25 ml) and $C_4H_9SnCl_3$ was added (2 mol.%). The solutions were stirred for 30 minutes and then atomised. The precursor flow was kept at 0.6 l.min^{-1}. The glass substrate was SiO_2 precoated (*ca.* 50 nm thick SiO_2 barrier layer) standard float glass (NSG) 15 cm × 4 cm × 0.3 cm. A top plate was suspended 0.5 cm above the glass substrate to ensure a laminar flow. The substrate was maintained at a temperature of 450 °C for a deposition time of 45 minutes. After the deposition the bubblers were closed and the substrates were cooled under a flow of nitrogen. The glass substrate was allowed to cool with the graphite block to less than 100 °C before it was removed. Coated substrates were handled and stored in air. The coated glass substrate was cut into ca. 1 cm × 1 cm squares for subsequent analysis.

Film Characterisation

Powder X-ray diffraction (PXRD) patterns were measured in a modified Bruker-Axs D8 diffractometer with parallel beam optics and a PSD LynxEye silicon strip detector. This instrument uses an unmonochromated Cu Kα source operated at 40 kV with 30 mA emission current. The incident beam angle was set at 1° and the angular range of the patterns collected was 10° < 2θ < 66° with a step size of 0.05° counted at 0.5s/step.

Scanning Electron Microscopy (SEM) was performed to determine surface morphology and film thickness using a JEOL JSM-6301F Field Emission SEM at an accelerating voltage of 5 keV.

Hall effect measurements were carried out using the van Der Pauw method to determine the bulk resistivity (ρ), sheet resistance, free carrier concentration (N) and mobility (μ). A square array of Ohmic contacts arranged on 1 cm^2 samples

were then subjected to an input current of 1 mA and a calibrated magnetic field of 0.58 T. The transverse voltage was then measured. The measurement was repeated by reversing the direction of the magnetic field and the current.

Optical spectra were taken using a Perkin Elmer Fourier transform Lambda 950 spectrometer over a wavelength range of 200 nm to 2250 nm (6.2 eV to 0.55 eV) in both transmission and reflection modes. This range embraces the ultraviolet (UV), visible and near infrared (NIR) regions. The spectra were referenced against an air background.

X-ray photoelectron spectroscopy (XPS) was performed in a Thermo Scientific K-alpha photoelectron spectrometer using monochromatic Al-K$_\alpha$ radiation. Survey scans were collected in the range 0–1100 eV (binding energy) at a pass energy of 160 eV. Higher resolution scans were recorded for the the main core lines at a pass energy of 20 eV. Valence band spectra were also recorded. Peak positions were calibrated using the C 1s peak and plotted using the CasaXPS software.

Mo/In K-edge X-ray absorption spectra (XAS) were measured on beam-line (B18) at the UK synchrotron, Diamond, which operates at 3 GeV and 300 mA. The beam line is equipped with Si(111) double crystal monochromator, ion chambers for measuring incident and transmitted beam intensity and a 9 element Ge fluorescence detector for measurement in fluorescence mode. All the measurements were carried out in fluorescence mode and typically 6 scans were averaged to produce the spectra. Spectra were processed using ATHENA software and subsequent analysis of the EXAFS data were performed using EXCURVE.[31,32]

Computational Methods

All our DFT calculations were performed using the VASP code,[21,22] with interactions between the cores (In:[Kr], Mo:[Xe] and O:[He]) and the valence electrons described using the PAW method.[34] The calculations were performed using the HSE06 hybrid functional as proposed by Krukau *et al.*[35] In the HSE06 approach, a value of exact nonlocal exchange, α, of 25%, and screening parameter of $\omega = 0.11$ bohr^{-1} are added to the Perdew Burke Ernzerhof PBE formalism. The HSE06 approach has been proven to result in structural and band gap data in better agreement with experiment than standard DFT functionals[8,36–39] and, crucially, to provide an excellent description of the electronic structure of In_2O_3. A planewave cutoff of 400 eV and a *k*-point sampling of *gamma*-centered 3×3×3 for the 40 atom primitive cell of In_2O_3 was used, with the structure deemed to be converged when the forces on all the atoms were less than 0.01 eV Å^{-1}.

All oxygen sites in the bixbyite structure are equivalent with four indium nearest-neighbours, whereas there are two distinct cation sites (8*b* and 24*d* in Wyckoff notation) that are each coordinated to 6 anions in distorted octahedra. One quarter of all the cations occupy the 8*b* position, with the remaining three quarters occupying the 24*d* positions. In ITO only tin doping on the indium *b*-sites results in active donors.[40,41] We have tested the incorporation of one Mo into the 40 atom primitive cell of In_2O_3 (i.e. replacing 6.25% of the In atoms) on both the 8*b* and 24*d* sites. Mo is 0.32 eV more stable on the 8*b* site, indicating that it will have a very strong preference at room temperature and above for taking up this site. Previously it was predicted that the 8*b* site was only 0.04 eV more favourable using the LDA method,[26] however, the discrepancy in these energy differences is as of yet unexplained. Nevertheless, the trend of Mo preferentially sitting on the 8*b* site is maintained. Our calculated lattice constants for cubic In_2O_3 is 10.16 Å,

which is within 0.40 % of the experimental lattice, while the calculated band gap at the HSE06 level is 2.75 eV in good agreement with experimental measurements [37].

3. Results and discussion

XRD, Hall effect, optical and SEM characterisation

The films deposited were uniform, showed excellent coverage across the glass substrates and were adherent, passing the Scotch tape test. X-ray diffraction patterns of the as-deposited films formed by AACVD (Figure 1) confirmed the presence of In_2O_3. The nominally undoped In_2O_3 films contained both the metastable rhombohedral In_2O_3 phase[42] as well as the cubic bixbyite In_2O_3 phase. When molybdenum was introduced into the system only the bixbyite In_2O_3 phase was observed. Molybdenum doping of In_2O_3 also resulted in pronounced (100) texture.
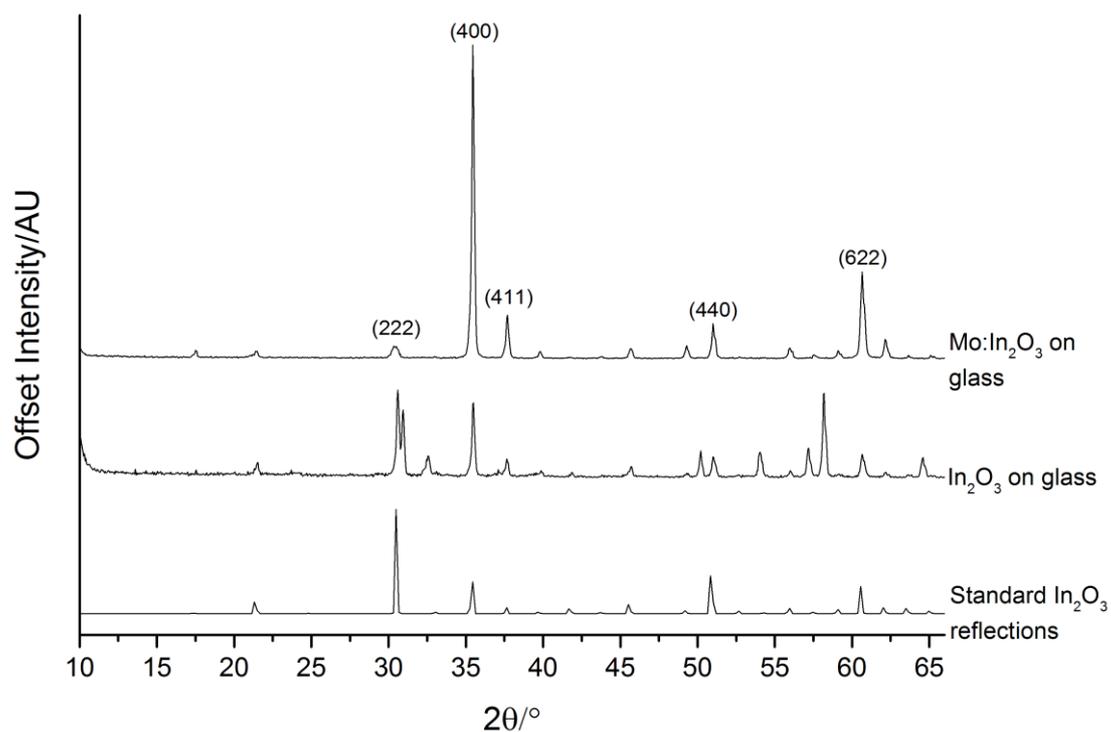
Figure 1. PXRD of nominally undoped In$_2$O$_3$ and Mo:In$_2$O$_3$ thin film samples prepared by the AACVD of InCl$_3$.xH$_2$O/(NH$_4$)$_6$Mo$_7$O$_{24}$.4H$_2$O with MeOH. Note the metastable rhombohedral In$_2$O$_3$ phase in nominally undoped In$_2$O$_3$ sample.

Mo:In or Sn:In in solution/mol. %	Film Thickness /nm	Sheet resistance/Ω.sq^{-1}	ρ/Ω.cm	μ/cm^2.V^{-1}.s^{-1}	N/cm^{-3}
0	700	11.0	7.7×10^{-4}	71	1.1×10^{20}
2 Sn	680	5.6	3.8×10^{-4}	25	6.7×10^{20}
1 Mo	610	3.1	1.9×10^{-4}	107	3.1×10^{20}
2 Mo	650	1.8	1.2×10^{-4}	119	4.4×10^{20}
3 Mo	650	1.8	1.2×10^{-4}	107	4.8×10^{20}
4 Mo	680	1.8	1.2×10^{-4}	92	6.5×10^{20}
5 Mo	680	1.2	8.3×10^{-5}	109	7.0×10^{20}
7 Mo	651	6.9	4.5×10^{-4}	45	3.1×10^{20}

Table 1. Film thickness, sheet resistance, specific resistivity, charge carrier mobility and charge carrier density of a nominally undoped In_2O_3 film, a $Sn:In_2O_3$ film and a series of $Mo:In_2O_3$ films.

The Hall effect measurements were performed at room temperature with the samples in van der Pauw configuration. The nominally undoped In_2O_3, $Sn:In_2O_3$ and $Mo:In_2O_3$ samples all showed n-type conductivity (table 1). The charge carrier mobility and charge carrier concentration for nominally undoped In_2O_3 were 71 cm^2/V.s and 1×10^{20} cm^{-3} respectively. The specific resistivity decreased with molybdenum doping as a consequence of an increase in both the charge carrier concentration and the charge carrier mobility. As shown in Figure 2, the carrier density increased to between 3.1×10^{20} cm^{-3} and 7.0×10^{20} cm^{-3} for between 1 and 5 mol.% Mo and the mobility increased to between 92 and 119 cm^2/V.s. The charge carrier concentrations in both nominally undoped In_2O_3 and $Mo:In_2O_3$ are much lower than in commercial ITO thin films, making them ideal for applications that require NIR transparency. The carrier density and mobility of an ITO film deposited by AACVD are also shown in Figure 2. Finally, the Hall effect results from the film prepared using 7 mol.% Mo in Figure 2 indicate a lower mobility of 45 $cm^2V^{-1}s^{-1}$ at the same carrier density as the 1 mol.% Mo film of 3.1×10^{20} cm^{-3}. This corresponds to overdoping with excess Mo atoms acting as acceptors, compensating the donors and giving an increased density of ionized impurities to scatter electrons and reduction of the mobility.
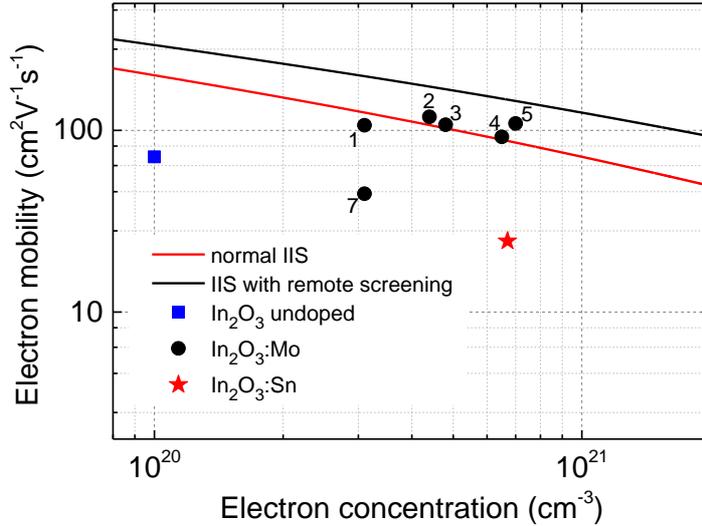
Figure 2: The electron mobility and concentration for undoped, Sn-doped and Mo-doped In$_2$O$_3$. The numbers by the data points correspond to the mol% of Mo dopant in the solution used in the AACVD. The model curves for regular ionized impurity scattering (IIS) (red line) and for remotely screened IIS (black line). All calculations are for singly ionized Mo donor atoms.

Also shown in Figure 2 is the ionized impurity scattering-limited mobility as a function of carrier density calculated using the Brooks-Herring-Dingle model[43] including degeneracy and conduction band non-parabolicity with a conduction band edge effective mass of 0.30m$_0$.[23] All calculations are for Mo donor atoms that are singly charged as justified by the DFT, XPS, and EXAFS results below. Ionized impurity scattering is dominant at carrier densities above 10^{20} cm^{-3}, but the mobility can be expected to be reduced slightly further by polar optical phonon scattering.[23] Two curves are shown - the lower mobility one which simply represents regular ionized impurity scattering and the higher mobility one which includes a factor accounting for "remote" impurities as described below. Four of the experimental data points correspond to mobilities higher than the regular ionized impurity scattering limit. This result alone implies that conventional ionized impurity scattering cannot account for the observed mobilities. If an

additional factor accounting for "remote" impurities is included, the higher mobility curve is obtained that is above all the experimental data points.

If the donor centre does not contribute significantly to the conduction band minimum, as is the case here for Mo as determined below from our DFT results, the amplitude of the conduction band wavefunction in the vicinity of the donor centre is small. Therefore, the conduction electrons do not experience scattering by the dopant's screened Coulomb potential to the same extent as in Sn-doped In_2O_3 where the Sn atoms do contribute significant orbital character to the bottom of the conduction band. In this sense, the Mo dopant atoms can be considered as being "remote" impurities, at least compared with the Sn atoms in ITO. This is also the case for La doped $BaSnO_3$ which exhibits high mobility as a result of the La orbitals lying several electron volts above the conduction band minimum rather than close in energy to it.[44]

To make a difference, the separation of the Mo donors from the indium atoms that do contribute to the conduction band minimum needs to be comparable to the Thomas-Fermi screening length. If the In atoms have a distance d from the Mo donor atoms that is comparable to the Thomas Fermi screening length, λ_{TF}, then the Coulomb interaction that produces ionised impurity scattering is reduced by a factor $\exp(-d/\lambda_{TF})$. To estimate the magnitude of this effect, we will consider the minimum Mo-In separation of 3.36 Å (see EXAFS results below), and Thomas-Fermi screening lengths of between 9.1 and 5.3 Å for carrier densities of between 8×10^{19} cm^{-3} and 2×10^{21} cm^{-3}. This gives Coulomb scattering of between 0.53 and 0.69 times what it would be for the case of regular impurities in this carrier density range. And the corresponding enhancements of the ionized impurity scattering limited mobility range from 1/0.69 = 1.4 to 1/0.53

= 1.9 times. The resulting mobility versus carrier density curve is shown as the black line in figure 2.

This situation is in part analogous to modulation doping of AlGaAs/GaAs heterostructures where the dopant atoms are located in the AlGaAs layers while the resulting conduction electrons flow through the spatially separated GaAs layer.[45] As a result, the electrons do not experience ionized impurity scattering by the dopants from which they originated. A similar but less dramatic spatial separation occurs in the current situation of the donor atom orbitals not contributing significantly to the bottom of the conduction band. Additionally, a different but related phenomenon has also been reported in nanoscale metal oxide semiconductor field effect transistors, whereby the ionized impurities in the channel are remotely screened by the close proximity of the highly doped, degenerate source and drain regions.[46]

The film microstructure and thickness was probed using SEM. The nominally undoped and molybdenum doped In_2O_3 films both displayed a similar microstructure based on pyramidal crystallites with a particle size of around 300 – 500 nm (Figure 3). The surface microstructure of these films make them potentially useful as electrodes in silicon based solar cells where there is a need to increase the path-length of incident light that can be achieved through optical scattering. The SEM of the 2 mol% Sn doped sample revealed similar sized grains as for the Mo doped samples but with inferior grain connectivity. The latter property probably accounts to some extent for the measured mobility for the Sn doped film being lower than the optimium achieved for polycrystalline ITO.
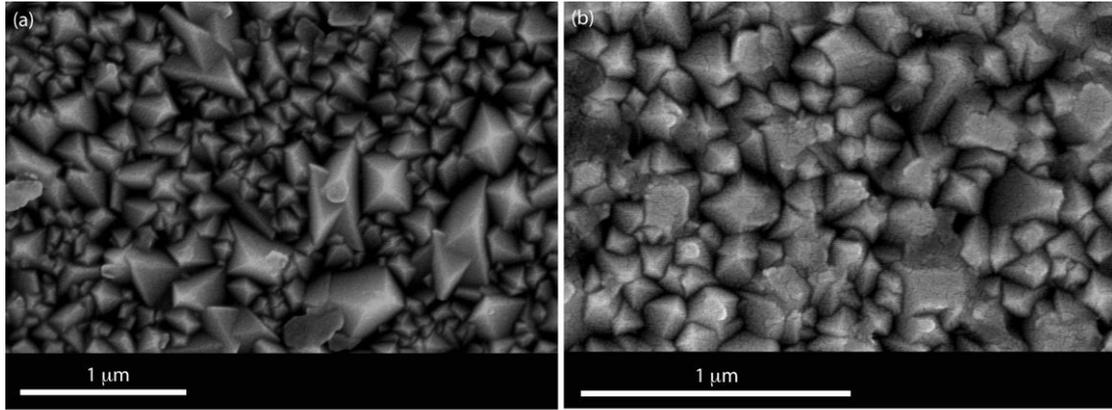
Figure 3. SEM images of (a) nominally undoped In_2O_3 and (b) $Mo:In_2O_3$ thin films deposited on silica coated float-glass substrates by the AACVD reaction of $InCl_3.xH_2O/(NH_4)_6Mo_7O_{24}.4H_2O$ and methanol at 450 °C.

Optical spectra across the UV, visible and near IR regions were collected for nominally undoped In_2O_3 and $Mo:In_2O_3$ thin films in transmittance and reflectance geometry between 250-2250 nm and are shown in figure 4. It can be seen that nominally undoped In_2O_3 films prepared within the AACVD system have a transmittance of up to 80% in the visible region with an average of ~ 75% between 400 – 2000 nm. Similar high NIR transmittance was previously observed in nominally undoped SnO_2 and In_2O_3 films having similar charge carrier concentrations but with considerably lower charge carrier mobilities.[47,48]

(a)

(b)
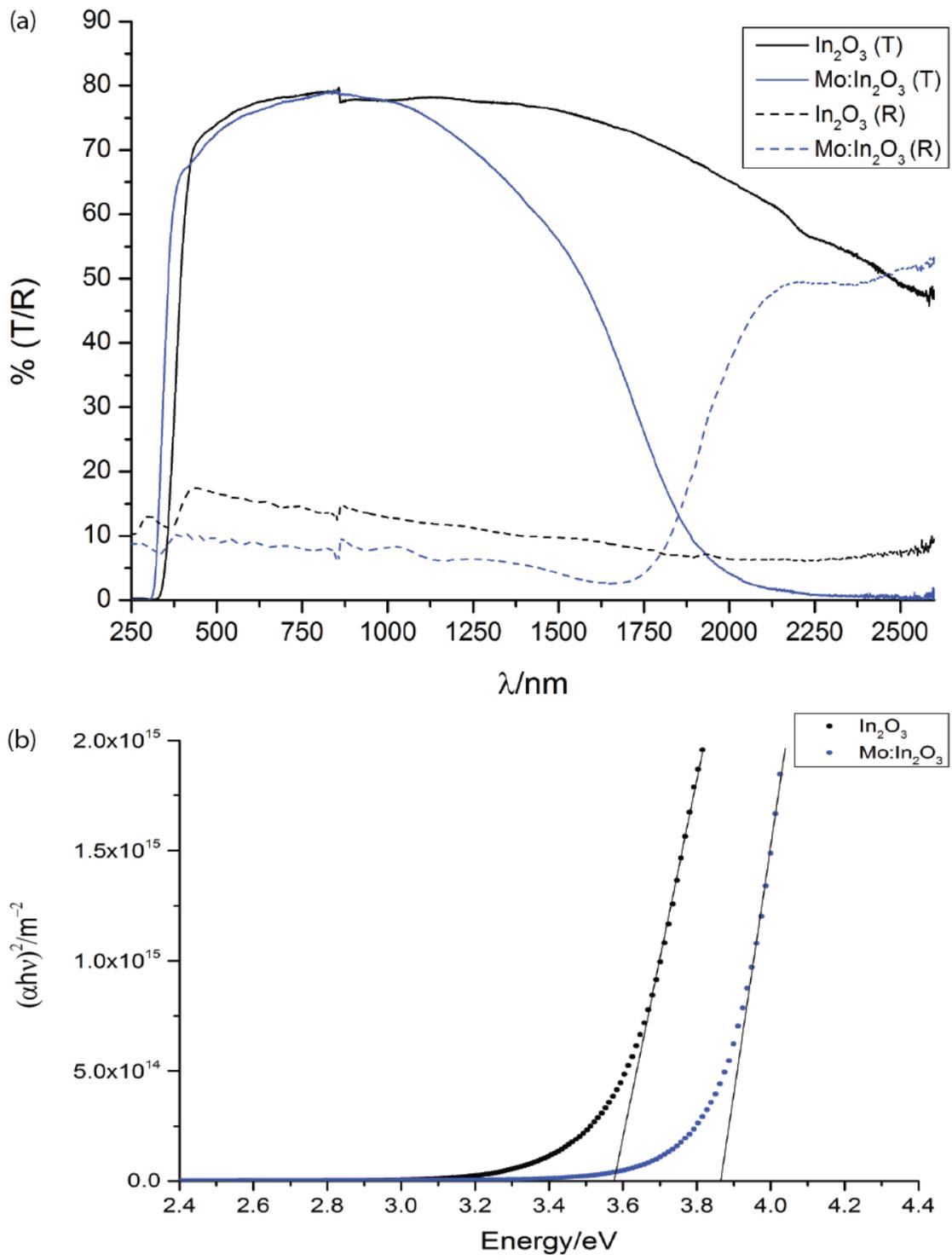
Figure 4. UV/vis spectra (T/R) of nominally undoped and Mo:In$_2$O$_3$ films prepared by the aerosol assisted chemical vapour deposition (AACVD) reaction of InCl$_3$.xH$_2$O/(NH$_4$)$_6$Mo$_7$O$_{24}$.4H$_2$O with MeOH on silica coated float glass substrates at 450 °C.

It is also evident from figure 4(a) that with molybdenum doping the transmittance in the visible region with wavelengths lower than 1000 nm (1.2 eV) remains essentially unaltered at just under 80%. The transmittance drops above 1000 nm in the IR due to increasing reflectivity and absorption on approaching and moving through the plasmon energy which is estimated, from the energy at which the reflectivity reaches half its maximum value, to be about 0.64 eV (1950 nm), in satisfactory agreement with the Hall carrier density. A similar carrier density may also be inferred from analysis of the In 3d core line (not shown) where final state structure due to final state screening and excitation of plasmon satellites is found.[49–51] In addition to the changes at long wavelength, Mo doping leads to a shift in the UV absorption onset to higher energy due to blocking of states at the bottom of the conduction band. Figure 4(b) shows the blue shift in a Tauc plot of $(\alpha h\nu)^2$ versus photon energy $h\nu$ is is from 3.55 to 3.85 eV, a shift of about 0.30 eV (here α is the absorption coefficient).[52,53] This is the size of expected when the carrier density increases from 1.1×10^{20} cm-3 to 4.4×10^{20} cm3, considering the influence of conduction band nonparaboclity.[54,55]

Density Functional Theory and Electronic Structure

The full and partial densities of states of both pure and Mo-doped In_2O_3 calculated using hybrid DFT are displayed in Figure 5 (a) and (b). The valence band of undoped In_2O_3 is dominated by O 2p states, hybridised with In 5s states at the bottom of the valence band, In 5p states in the middle of the band and In 4d states at the top of the band. The bottom of the conduction band is of dominant In 5s character but with strong hybridisation with O 2p states. The experimental band gap of 2.9 eV[55] is reproduced quite well by the calculation, which gives a value of

2.75 eV. Mo doping shifts the Fermi level up above the conduction band minimum (CBM) but also introduces new Mo 4d states into the bulk band gap. Moreover there is no shrinkage in the energy between the CBM and the valence band minimum (VBM). Looking at the band structure itself (figure 6) we find that undoped In_2O_3 has a strongly dispersing conduction band with a minimum at the Γ point and a VBM composed of relatively flat bands. For Mo-doped In_2O_3 additional states of dominant Mo 4d character appear both above and below the CBM. Specifically two localized t_{2g} α-spin (spin-up) states are found in the band gap below the CBM, while the β-spin t_{2g} state lies above the CBM at the Γ point. This indicates that Mo is only donating 1 electron to the conduction band. Thus in *bulk* In_2O_3 the Mo dopant is 4+, and not 6+ as had been previously postulated.[24,56] In addition, careful analysis of the contribution of Mo states to the conduction band revealed that at the Γ point the Mo contribution to states at the CBM is less than 3%. The flat band above that has 74% Mo character, indicating that the Mo states lie above the CBM, but with very little hybridization with the CBM. The Mo donates one electron but does not get involved in the conduction band, therefore conduction electrons do not scatter off the dopant centre in the way that is the case for Sn doped In_2O_3 where the conduction band minimum has a very strong contribution (10% for the same unit cell) from Sn 5s states.[57]

Mo-doping of In_2O_3 has been examined previously by Medvedeva using computational methods, with the conclusion that Mo acts as a three electron donor.[26] However, this study used the local density approximation (LDA) approach, which suffers from a severe band gap error and has been shown to erroneously favour delocalized electrons in semiconductors. A hybrid-DFT

approach such as the HSE06 functional employed here rectifies these problems and yields a far more realistic electronic structure of a doped In_2O_3.[58,59]
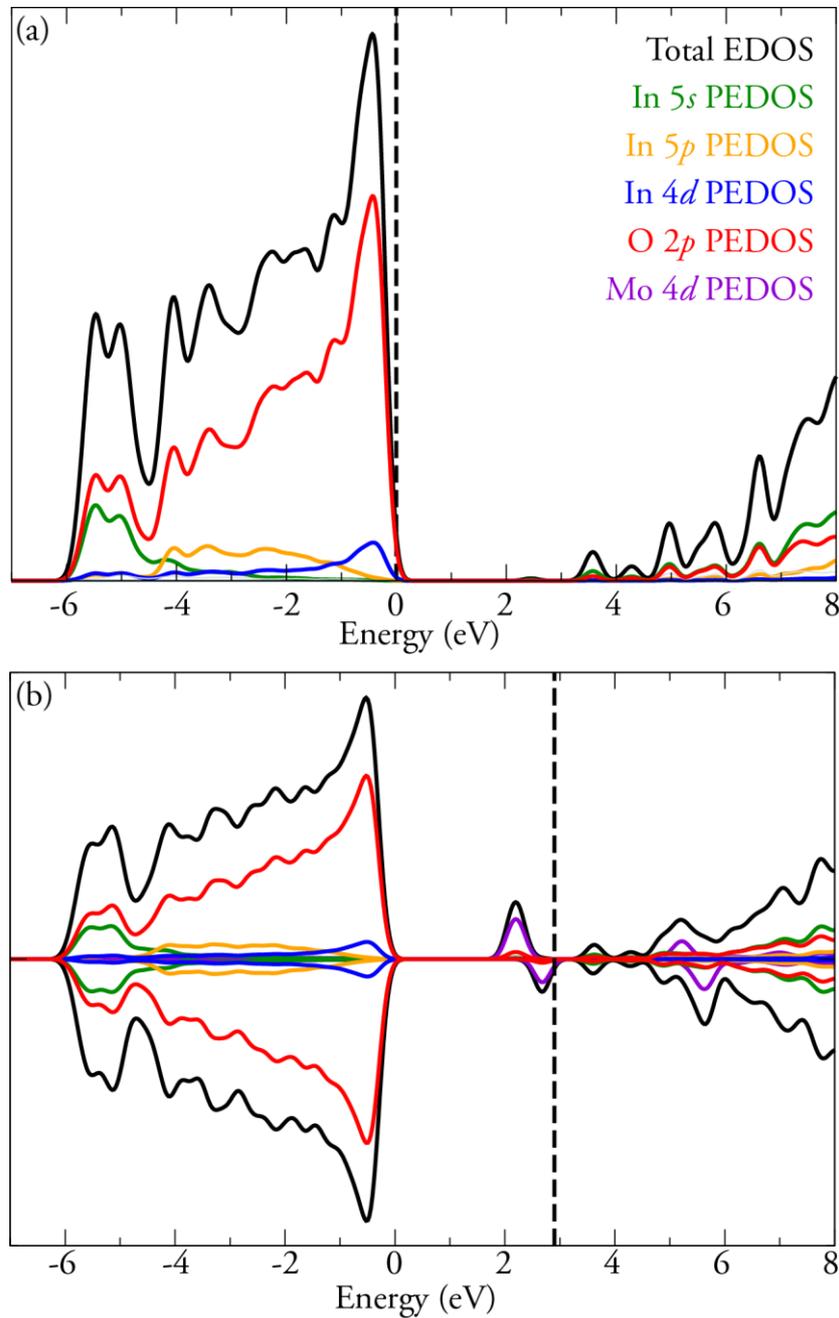
Figure 5. HSE06 calculated total and partial energetic density of states for (a) pure In_2O_3 and (b) one Mo dopant on the 8b site in a 40 atom primitive cell corresponding to a carrier density of about 1.9 x10^{21} cm³. The valence band maximum is set to 0 eV. The dashed lines indicate the highest occupied states.
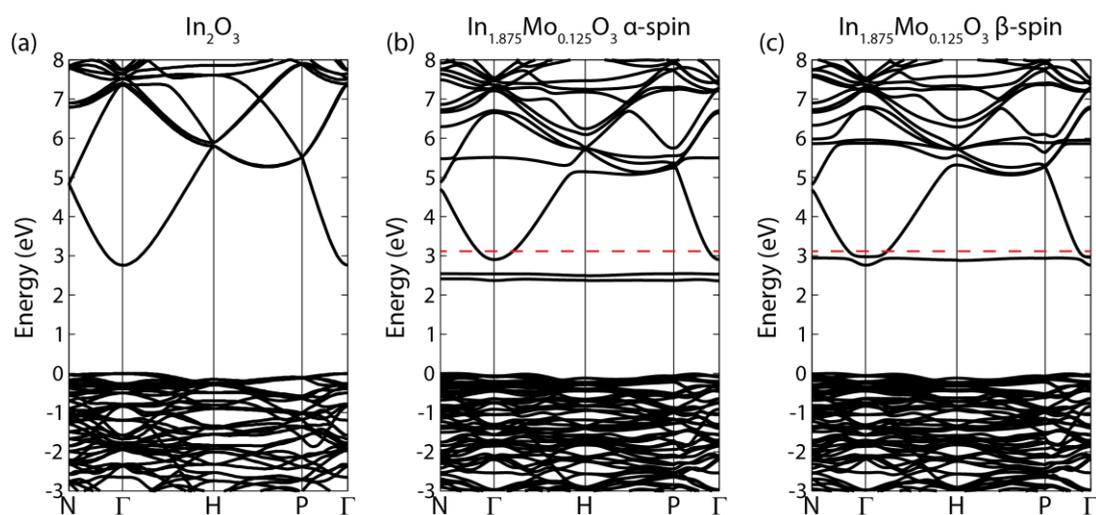
Figure 6. HSE06 calculated band structures for (a) pure In₂O₃, (b) spin up states for one Mo dopant on the 8b site in a 40 atom primitive cell and (c) spin down states for one Mo dopant on the 8b site in a 40 atom primitive cell. The valence band maximum is set to 0 eV. The dashed red lines indicate the highest occupied states.

Valence band XPS

Valence band X-ray photoemission spectra are shown in figure 7. The spectra are dominated by a broad valence band of O 2p states extending from the valence band onset to about 10 eV binding energy.

The valence band positions cannot simply be derived by linear extrapolation of the rising edge of the valence band to the baseline. It has been shown[42] that that there is a rapid onset of the valence band density of states leading to an almost flat band. Broadening due to lifetime and instrument effects causes significant slope to the measured onset of the valence band. Therefore extrapolating to the baseline results in a large underestimation in the VBM to surface Fermi level separation.

The shift of the onsets to higher binding energy for Mo-doped In₂O₃ is indicative of population of the conduction band by excess charge carriers introduced by

molybdenum doping and is analogous to the Burstein-Moss shift in optical spectra. More importantly the valence band photoemission data shows occupied states in the bandgap, consistent with the computational results discussed above which revealed the presence of occupied localised Mo 4d states.
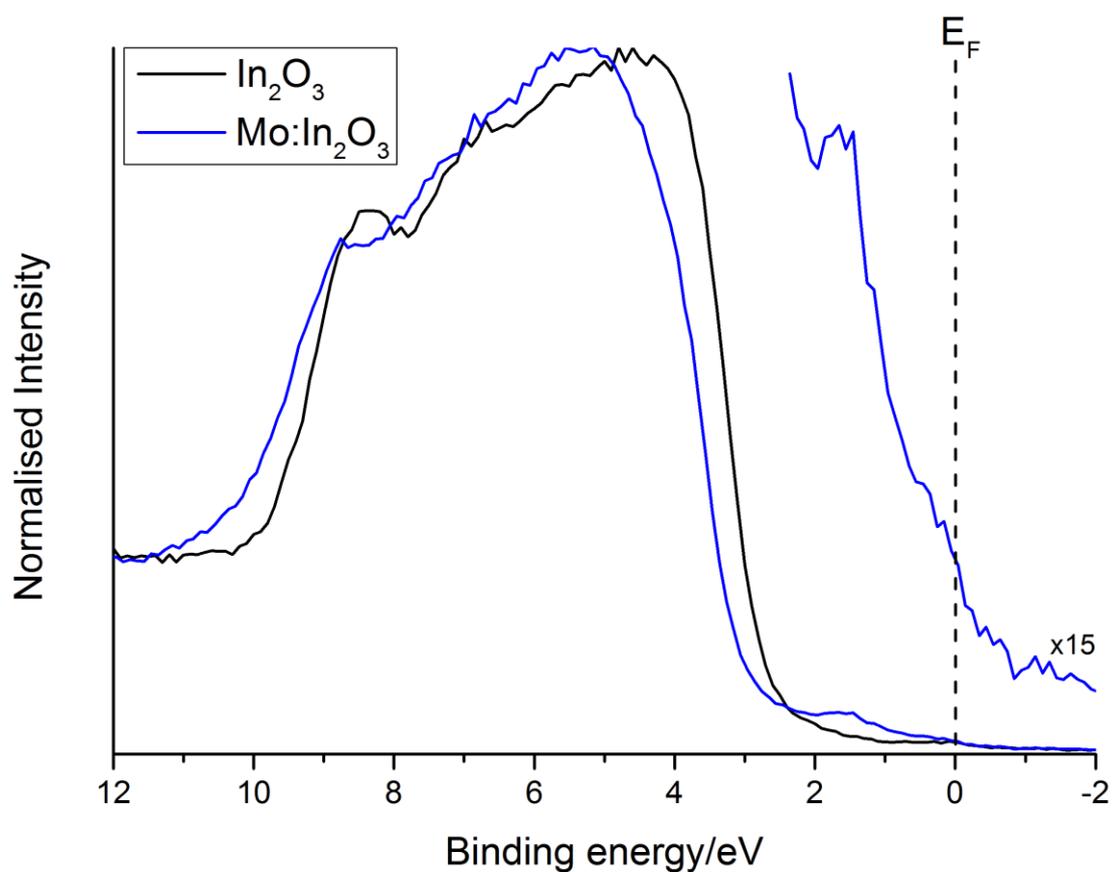
Figure 7. Normalised valence-band photoemission spectrum of nominally undoped In_2O_3 and $Mo:In_2O_3$ thin films deposited on glass substrates. Note the shift to higher binding energy for the $Mo:In_2O_3$ sample due to Burstein-Moss filling of the conduction band. Also the $Mo:In_2O_3$ sample shows Mo 4d states in the band gap consistent with computational results.

Mo core level spectroscopy.

21

Figure 8 shows the core photoemission spectrum the sample doped with 2% Mo in solution in the Mo 3d region. The effective Mo doping level in the near surface region was found to be 0.9%, corresponding to a Mo concentration of 3 x 10^{20} cm^{-3}. Within the experimental uncertainty this corresponds to the difference in carrier density between the nominally undoped and the doped films, strongly suggesting that Mo acts as 1 electron donor. To explore this idea further the Mo $3d_{5/2}$ and Mo $3d_{3/2}$ components of the spin-orbit doublet were each fitted with a pair of Voigt functions superimposed on a Shirley background.[20,24,60–63] The high binding energy component found at 232.5 eV is at a similar energy to the value of 232.5 eV found in MoO_3[60] so the presence of Mo^{6+} in the near surface region can be inferred. This probably arises simply from oxidation of Mo close to the surface: similar contaminant structure has been observed for as-presented MoO_2 and may be removed by extended annealing in UHV. Identification of the charge state associated with the low binding energy component is more problematic, although comparison may be made with MoO_2. The Mo 3d spectrum of this metallic oxide is complicated by final state screening by the very high density of mobile charge carriers giving a doublet of doublets with a shift of 1.73 eV between screened and unscreened peaks.[60] The binding energy of 231.3 eV found in the present work is very close to the value of 231.0 eV for the unscreened final state observed for MoO_2. Of course in IMO one might anticipate a superposition of screened and unscreened components similar to that found in the In 3d region. However as was discussed above Mo 4d states contribute very little to the conduction band and in this situation there will be minimal local final state screening of a Mo core hole, resulting in the absence of the screened Mo^{4+} component. Therefore, the lower binding energy doublet in figure 8 is attributed to unscreened Mo^{4+} states and the

higher binding energy doublet to conventional Mo^{6+} states associated with oxidized Mo at the surface.
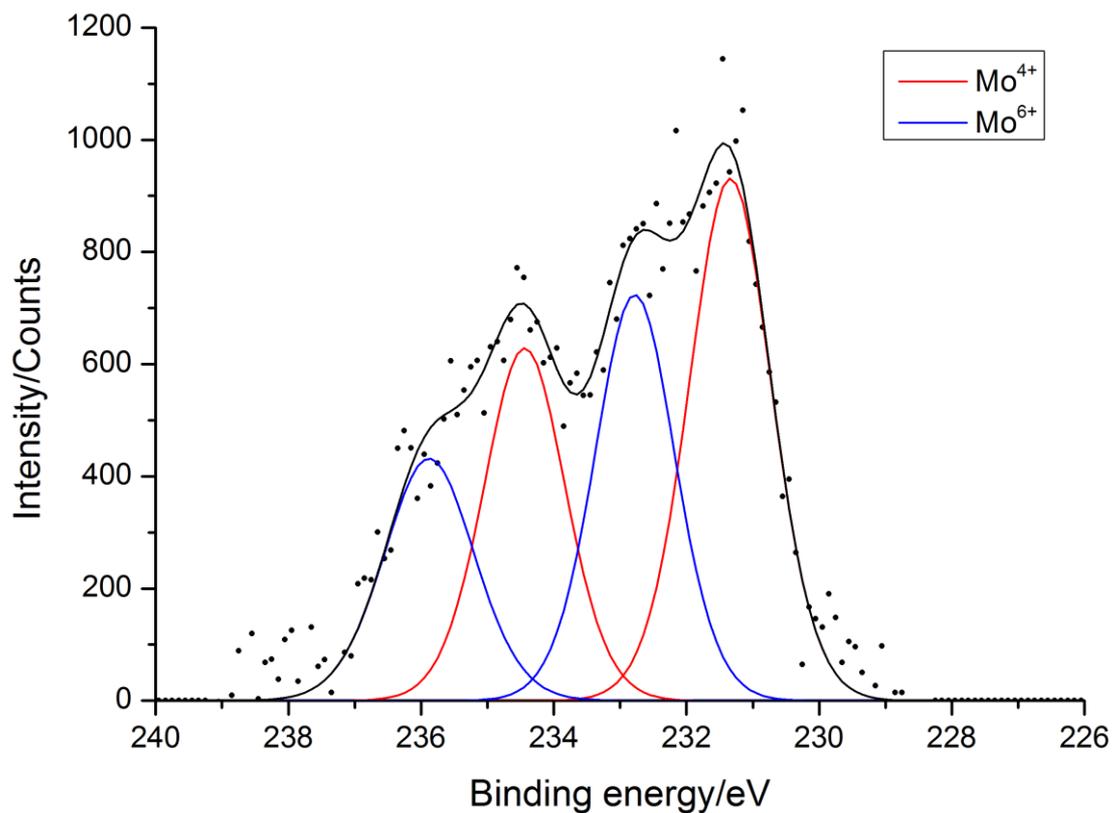
Figure 8. Mo $3d$ core level x-ray photoemission spectra of Mo:In$_2$O$_3$ film prepared from the AACVD reaction of InCl$_3$.xH$_2$O/(NH$_4$)$_6$Mo$_7$O$_{24}$.4H$_2$O and methanol. The dots represent experimental data points and the solid lines are best fits to the data. The data was fitted with a Shirley background and Voigt components for the Mo^{4+}/Mo^{6+} environments.

X-ray absorption spectroscopy.

XAS was used as an additional probe of the electronic and geometric state of molybdenum atoms in $Mo:In_2O_3$ in the bulk of the material. Whilst XPS measures tens of atomic layers into the sample, XAS is an atom specific technique used to probe the bulk short-range structure. Figure 9 shows the Mo K-edge XANES for $Mo:In_2O_3$ thin film, MoO_2 and MoO_3 model compounds. It can clearly be seen that for MoO_3 there is a clear pre-edge feature at *ca.* 20008 eV. The intensity of this pre-edge feature depends on the coordination around the metal centre. The pre-edge intensity is greater for metal ions with tetrahedral coordination compared to octahedral coordination. The pre-edge intensity also depends on the electronic structure of the metal ions in a given oxidation state, for example d^0 systems showing a more intense pre-edge feature.[64,65] The MoO_2 model compound and $Mo:In_2O_3$ do not exhibit this pre-edge feature implying that Mo in $Mo:In_2O_3$ is doping in the system as Mo^{4+} consistent again with photoemission and theoretical results.
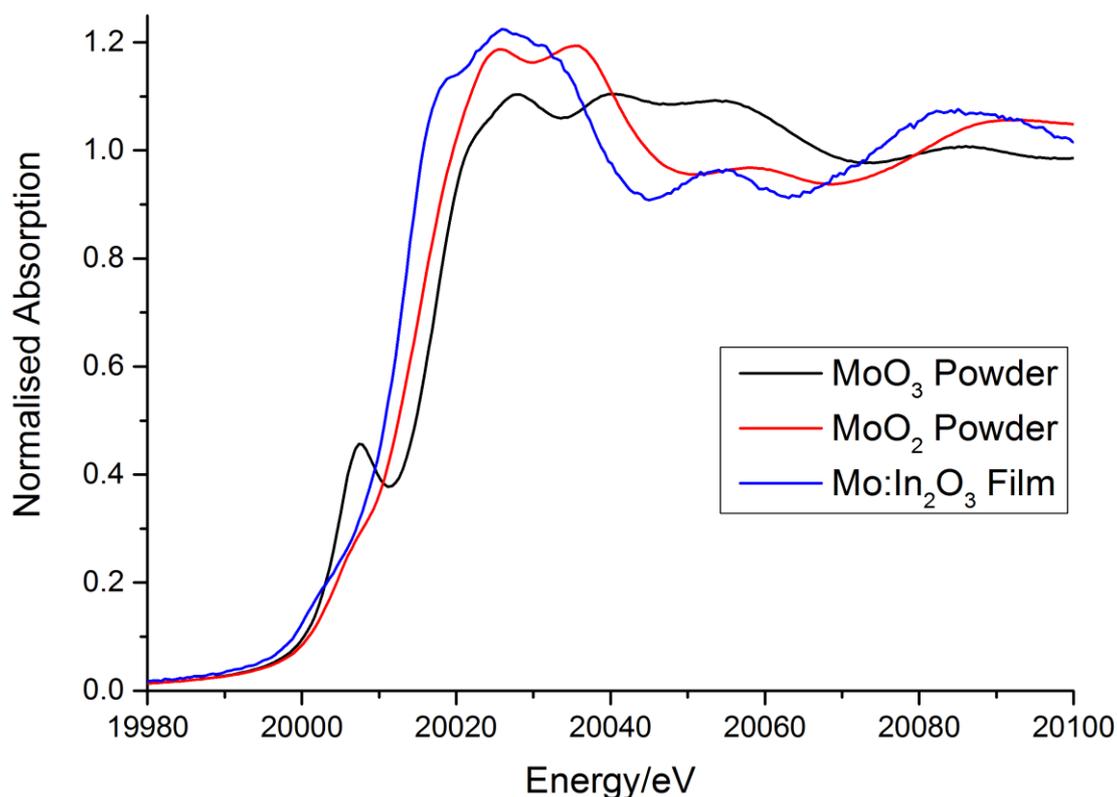
Figure 9. Mo K-edge XANES of Mo:In₂O₃ (2 mol.% in solution) thin film and corresponding model compounds.

Analysis of the Mo K-edge EXAFS data revealed that the average Mo-O distance of the first neighbour in Mo:In2O3 thin film is *ca* 2.05 Å, shorter than the In-O distance in In$_2$O$_3$ of ca 2.16 Å, due to the smaller ionic radius of Mo^{4+} in comparison to In^{3+}. Importantly the bond distance is more similar to MoO$_2$ and significantly different from MoO$_3$ indicating no phase segregation to MoO$_2$/MoO$_3$. More striking differences between the structure of MoO$_2$ and the doped materials can be seen in the second and third neighbour distances; Mo-In distances were found to be similar to that observed for In-In in In$_2$O$_3$ which is very different from MoO$_2$. The results of the analysis are given in Table 2 and the best fit between experimental data and the calculated Mo K-edge EXAFS along with the associated Fourier

transforms of Mo:In$_2$O$_3$ system are shown in Figure 10. These results clearly provide a direct evidence for the substitution of Mo^{4+} ions in the In$_2$O$_3$ lattice.

System	Atom Pair	N–Coordination number	R (Å) – Interatomic distance	σ² (Å²) – Debye-Waller
Mo:In$_2$O$_3$	Mo-O	6.4	2.05	0.012
	Mo-In	6.0	3.36	0.004
	Mo-In	6.0	3.82	0.006
In$_2$O$_3$	In-O	6	2.16	0.005
	In-In	6	3.36	0.005
	In-In	6	3.87	0.007

Table 2. Structural Parameters Obtained from the Analysis of Mo K-edge EXAFS data on Mo:In$_2$O$_3$ film.
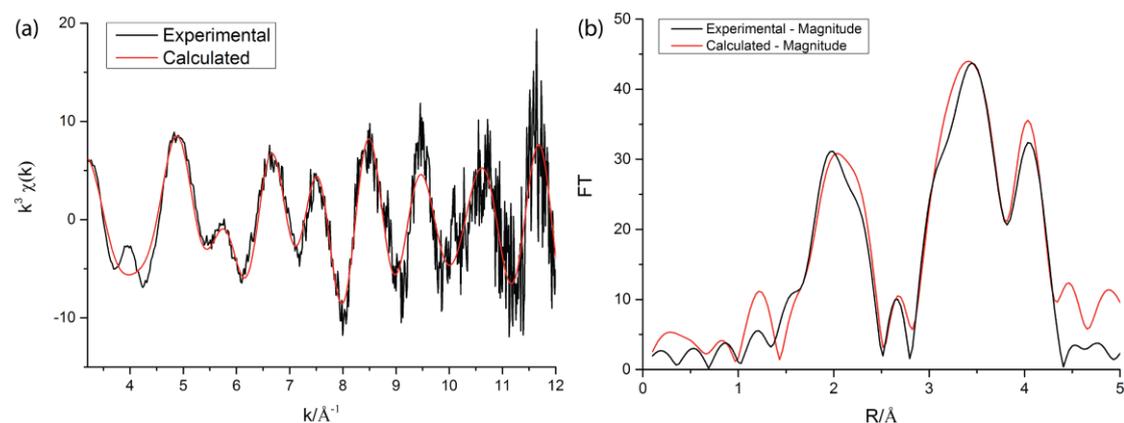
Figure 10. Mo K-edge EXAFS for Mo:In$_2$O$_3$ film (a) and associated Fourier transforms showing experimental and calculated data for real and imaginary components (b).

Conclusions

AACVD was shown to be an effective method for the deposition of In_2O_3 and $Mo:In_2O_3$ thin films deposited on silica coated float glass *via* the AACVD reaction of unconventional CVD precursors $InCl_3.xH_2O/(NH_4)_6Mo_7O_{24}.4H_2O$ and methanol at a substrate temperature of 450 °C. Nominally undoped In_2O_3 thin films gave surprisingly high charge carrier concentrations (1×10^{20} cm^{-3}) and charge carrier mobilities (71 $cm^2/V.s$) comparable and superior to some intentionally doped In_2O_3. Molybdenum was substitutionally incorporated into the In_2O_3 structure and resulted in an increase in the charge carrier concentration to 4×10^{20} cm^{-3} with a concomitant increase in the charge carrier mobility to 119 $cm^2/V.s$, without a decrease in the average transmittance in the visible/NIR region. In $Mo:In_2O_3$, as the dopant density increased the charge carrier mobility increased also. Hybrid-DFT calculations showed the molybdenum states exist high up in the conduction band but the hybridisation of Mo states to the CBM was low, thus the conduction band electrons do not get scattered off the dopant centre in the way that is the case for Sn doped In_2O_3. This case is analogous to that of, $La:BaSnO_3$[44], where the La donor states also appear high in the conduction band, meaning that the CBM is unchanged relative to pure $BaSnO_3$, which is most likely the source of the extremely high mobilities reported for single crystal and thin films,[44,66–68] thus, through a combination of XPS, XAS and DFT calculations we have explained the oxidation state of $Mo:In_2O_3$ and the nature of the high electron mobility observed in $Mo:In_2O_3$

References

(1) Hamberg, I.; Granqvist, C. G. *Journal of Applied Physics* **1986**, *60*, R123.
(2) Mayer, B. *Thin Solid Films* **1992**, *221*, 166–182.
(3) Kuang, D.; Uchida, S.; Humphry-Baker, R.; Zakeeruddin, S. M.; Grätzel, M. *Angewandte Chemie International Edition* **2008**, *47*, 1923–1927.
(4) Gratzel, M. *Inorganic Chemistry* **2005**, *44*, 6841–6851.
(5) Mishima, T.; Taguchi, M.; Sakata, H.; Maruyama, E. *Solar Energy Materials and Solar Cells* **2011**, *95*, 18–21.
(6) Yano, A.; Tohoda, S.; Matsuyama, K.; Nakamura, Y.; Nishiwaki, T.; Fujita, K.; Taguchi, M.; Maruyama, E. **2013**.
(7) Walsh, A.; Da Silva, J. L. F.; Wei, S.-H. *Journal of Physics: Condensed Matter* **2011**, *23*, 334210.
(8) Scanlon, D. O.; Kehoe, A. B.; Watson, G. W.; Jones, M. O.; David, W. I. F.; Payne, D. J.; Egdell, R. G.; Edwards, P. P.; Walsh, A. *Physical Review Letters* **2011**, *107*.
(9) Bierwagen, O.; Speck, J. S. *Journal of Applied Physics* **2010**, *107*, 113519.
(10) Edwards, P. P.; Porch, A.; Jones, M. O.; Morgan, D. V.; Perks, R. M. *Dalton Transactions* **2004**, 2995.
(11) Coutts, T. J.; Young, D. L.; Li, X. *MRS Bulletin* **2011**, *25*, 58–65.
(12) Exarhos, G. J.; Zhou, X.-D. *Thin Solid Films* **2007**, *515*, 7025–7052.
(13) Ginley, D. S.; Bright, C. *MRS Bulletin* **2011**, *25*, 15–18.
(14) Gordon, R. G. *MRS Bulletin* **2011**, *25*, 52–57.

(15) Granqvist, C. G. *Solar Energy Materials and Solar Cells* **2007**, *91*, 1529–1598.

(16) Hartnagel, H. L.; Dawar, A. L.; Jain, A. K.; Jagadish, C. *Semiconducting Transparent Thin Films*; IOP Publishing Ltd, 1995.

(17) Gupta, R. K.; Ghosh, K.; Mishra, S. R.; Kahol, P. K. *Applied Surface Science* **2008**, *254*, 4018–4023.

(18) Gupta, R.; Ghosh, K.; Mishra, S. R.; Kahol, P. K. *MRS Proceedings* **2007**, *1030*.

(19) Lozano, O.; Chen, Q. Y.; Wadekar, P. V.; Seo, H. W.; Chinta, P. V.; Chu, L. H.; Tu, L. W.; Lo, I.; Yeh, S. W.; Ho, N. J.; Chuang, F. C.; Jang, D. J.; Wijesundera, D.; Chu, W.-K. *Solar Energy Materials and Solar Cells* **2013**, *113*, 171–178.

(20) Warmsingh, C. *Journal of Applied Physics* **2004**, *95*, 3831.

(21) Gupta, R. K.; Ghosh, K.; Mishra, S. R.; Kahol, P. K. *Materials Letters* **2008**, *62*, 1033–1035.

(22) Van Hest, M. F. A. M.; Dabney, M. S.; Perkins, J. D.; Ginley, D. S.; Taylor, M. P. *Applied Physics Letters* **2005**, *87*, 032111.

(23) Preissler, N.; Bierwagen, O.; Ramu, A. T.; Speck, J. S. *Physical Review B* **2013**, *88*.

(24) Yoshida, Y.; Wood, D. M.; Gessert, T. A.; Coutts, T. J. *Applied Physics Letters* **2004**, *84*, 2097.

(25) Rauch, C.; Tuomisto, F.; King, P. D. C.; Veal, T. D.; Lu, H.; Schaff, W. J. *Applied Physics Letters* **2012**, *101*, 011903.

(26) Medvedeva, J. *Physical Review Letters* **2006**, *97*.

(27) Hassan, I. A.; Ratnasothy, A.; Bhachu, D. S.; Sathasivam, S.; Carmalt, C. J. *Australian Journal of Chemistry* **2013**.

(28) Bhachu, D. S.; Sankar, G.; Parkin, I. P. *Chemistry of Materials* **2012**, *24*, 4704–4710.

(29) Sathasivam, S.; Arnepalli, R. R.; Kumar, B.; Singh, K. K.; Visser, R. J.; Blackman, C. S.; Carmalt, C. J. *Chemistry of Materials* **2014**, *26*, 4419–4424.

(30) Nishinaka, H.; Kamada, Y.; Kameyama, N.; Fujita, S. *Japanese Journal of Applied Physics* **2009**, *48*, 121103.

(31) Ravel, B.; Newville, M. *Journal of Synchrotron Radiation* **2005**, *12*, 537–541.

(32) Gurman, S. J.; Binsted, N.; Ross, I. *Journal of Physics C: Solid State Physics* **1986**, *19*, 1845–1861.

(33) Kresse, G.; Hafner, J. *Physical Review B* **1994**, *49*, 14251–14269.

(34) Kresse, G. *Physical Review B* **1999**, *59*, 1758–1775.

(35) Krukau, A. V.; Vydrov, O. A.; Izmaylov, A. F.; Scuseria, G. E. *The Journal of Chemical Physics* **2006**, *125*, 224106.

(36) Burbano, M.; Scanlon, D. O.; Watson, G. W. *Journal of the American Chemical Society* **2011**, *133*, 15065–15072.

(37) Allen, J. P.; Scanlon, D. O.; Watson, G. W. *Physical Review B* **2010**, *81*.

(38) Scanlon, D. O.; Watson, G. W. *Journal of Materials Chemistry* **2011**, *21*, 3655.

(39) Ãgoston, P.; Albe, K.; Nieminen, R. M.; Puska, M. J. *Physical Review Letters* **2009**, *103*.

(40) González, G. B.; Cohen, J. B.; Hwang, J.-H.; Mason, T. O.; Hodges, J. P.; Jorgensen, J. D. *Journal of Applied Physics* **2001**, *89*, 2550.

(41) Binczycka, H.; Uhrmacher, M.; Elidrissi-Moubtassim, M. L.; Jumas, J.-C.; Schaaf, P. *physica status solidi (b)* **2005**, *242*, 1100–1107.

(42) King, P.; Veal, T. D.; Fuchs, F.; Wang, C. Y.; Payne, D.; Bourlange, A.; Zhang, H.; Bell, G. R.; Cimalla, V.; Ambacher, O.; others. *Physical Review B* **2009**, *79*, 205211.

(43) Look, D. C.; Lu, H.; Schaff, W. J.; Jasinski, J.; Liliental-Weber, Z. *Applied Physics Letters* **2002**, *80*, 258.

(44) Scanlon, D. O. *Physical Review B* **2013**, *87*.

(45) Dingle, R.; Störmer, H. L.; Gossard, A. C.; Wiegmann, W. *Applied Physics Letters* **1978**, *33*, 665.

(46) Towie, E. A.; Watling, J. R.; Barker, J. R. *Semiconductor Science and Technology* **2011**, *26*, 055008.

(47) Bel Hadj Tahar, R.; Ban, T.; Ohya, Y.; Takahashi, Y. *Journal of Applied Physics* **1998**, *83*, 2631.

(48) Bourlange, A.; Payne, D. J.; Palgrave, R. G.; Zhang, H.; Foord, J. S.; Egdell, R. G.; Jacobs, R. M. J.; Veal, T. D.; King, P. D. C.; McConville, C. F. *Journal of Applied Physics* **2009**, *106*, 013703.

(49) Egdell, R.; Rebane, J.; Walker, T.; Law, D. *Physical Review B* **1999**, *59*, 1792–1799.

(50) Christou, V.; Etchells, M.; Renault, O.; Dobson, P.; Salata, O.; Beamson, G.; Egdell, R. *Journal of Applied Physics* **2000**, *88*, 5180–5187.

(51) Körber, C.; Krishnakumar, V.; Klein, A.; Panaccione, G.; Torelli, P.; Walsh, A.; Da Silva, J. L. F.; Wei, S.-H.; Egdell, R. G.; Payne, D. J. *Physical Review B* **2010**, *81*.

(52) Tauc, J.; Grigorovici, R.; Vancu, A. *physica status solidi (b)* **1966**, *15*, 627–637.

(53) Tauc, J. *Materials Research Bulletin* **1968**, *3*, 37–46.

(54) Fuchs, F.; Bechstedt, F. *Physical Review B* **2008**, *77*.

(55) Walsh, A.; Da Silva, J. L.; Wei, S.-H.; Körber, C.; Klein, A.; Piper, L.; DeMasi, A.; Smith, K. E.; Panaccione, G.; Torelli, P.; others. *Physical review letters* **2008**, *100*, 167402.

(56) Meng, Y. *Thin Solid Films* **2001**, *394*, 218–222.

(57) Walsh, A.; Da Silva, J.; Wei, S.-H. *Physical Review B* **2008**, *78*.

(58) Scanlon, D. O.; Regoutz, A.; Egdell, R. G.; Morgan, D. J.; Watson, G. W. *Applied Physics Letters* **2013**, *103*, 262108.

(59) Walsh, A.; Scanlon, D. O. *Physical Review B* **2013**, *88*.

(60) Scanlon, D. O.; Watson, G. W.; Payne, D.; Atkinson, G.; Egdell, R.; Law, D. *The Journal of Physical Chemistry C* **2010**, *114*, 4636–4645.

(61) Chen, H.-Y.; Su, H.-C.; Chen, C.-H.; Liu, K.-L.; Tsai, C.-M.; Yen, S.-J.; Yew, T.-R. *Journal of Materials Chemistry* **2011**, *21*, 5745.

(62) Wu, C.; Shen, J.; Ma, J.; Wang, S.; Zhang, Z.; Yang, X. *Semiconductor Science and Technology* **2009**, *24*, 125012.

(63) Van Hest, M. F. A. M.; Dabney, M. S.; Perkins, J. D.; Ginley, D. S. *Thin Solid Films* **2006**, *496*, 70–74.

(64) Beale, A. M.; Sankar, G. *Chemistry of Materials* **2003**, *15*, 146–153.

(65) Corma, A.; Rey, F.; Thomas, J. M.; Sankar, G.; Greaves, G. N.; Cervilla, A.; Llopis, E.; Ribeira, A. *Chemical Communications* **1996**, 1613.

(66) Sallis, S.; Scanlon, D. O.; Chae, S. C.; Quackenbush, N. F.; Fischer, D. A.; Woicik, J. C.; Guo, J.-H.; Cheong, S. W.; Piper, L. F. J. *Applied Physics Letters* **2013**, *103*, 042105.

(67)   Kim, H. J.; Kim, U.; Kim, T. H.; Kim, J.; Kim, H. M.; Jeon, B.-G.; Lee, W.-J.; Mun, H. S.; Hong, K. T.; Yu, J.; Char, K.; Kim, K. H. *Physical Review B* **2012**, *86*.

(68)   Kim, H. J.; Kim, U.; Kim, H. M.; Kim, T. H.; Mun, H. S.; Jeon, B.-G.; Hong, K. T.; Lee, W.-J.; Ju, C.; Kim, K. H.; Char, K. *Applied Physics Express* **2012**, *5*, 061102.